Received: Added at production | Revised: Added at production | Accepted: Added at production

DOI: xxx/xxxx

ARTICLE TYPE

A data-driven model for endoplasmic reticulum membrane compartmentalization in budding yeast cells

Aymen Laadhari*[1] | Yves Barral[2] | Gabor Székely[3]

[1]Department of Mathematics, Khalifa University, Abu Dhabi, United Arab Emirates

[2]Department of Biology, Swiss Federal Institute of Technology ETH Zürich, HPM D 8.3, Otto-Stern-Weg 3, CH-8093 Zürich, Switzerland

[3]Department of Information Technology and Electrical Engineering, Swiss Federal Institute of Technology ETH Zürich, Sternwartstrasse 7, CH-8092 Zürich, Switzerland

Correspondence
*Email: Aymen.Laadhari@ku.ac.ae

Summary

We present a framework to model and provide numerical evidence for compartmentalization in the yeast endoplasmic reticulum. Measurement data is collected and an optimal control problem is formulated as a regularized inverse problem. To our knowledge, this is the first attempt in the literature to introduce a PDE-constrained optimization formulation to study the kinetics of fluorescently labeled molecules in budding yeast. Optimality conditions are derived and a gradient descent algorithm allows accurate estimation of unknown key parameters in different cellular compartments. For the first time, the numerical results support the empirical barrier index theory suggesting the presence of a physical diffusion barrier that compartmentalizes the endoplasmic reticulum by limiting protein exchange between the mother and its growing bud. We report several numerical experiments on real data and geometry, with the aim of illustrating the accuracy and efficiency of the method. Furthermore, a relationship between the size ratio of mother and bud compartments and the barrier index ratio is provided.

KEYWORDS:
Optimal control, optimize then discretize, surface PDE, finite element method, yeast cell, diffusion barrier

1 | INTRODUCTION

In budding yeast cells, a small daughter cell emerges from the mother cell, which can produce nearly 20-50 rejuvenated daughters before it dies. The endoplasmic reticulum, referred to as ER, of the budding yeast cell is made up of membranous tubules and sheet-like cisterns. The principles underlying the anisotropic protein exchange in budding yeast have been the subject of several experimental studies showing that this is not due to the geometric organization of the ER, see [1,2,3,4]. The membrane of the endoplasmic reticulum is composed of morphologically and functionally diverse domains, such as rough ER, smooth ER and nuclear envelope, whose distinction is based on the contribution of several proteins [5]. It can be divided into large compartments roughly corresponding to the future daughter cells covering the mother compartment Γ_m which includes the nuclear envelope and is larger than the bud region Γ_b; The bud neck zone Γ_r, however, has a sheet morphology instead of tubules [5], see Fig.1. In budding yeast cells as well as in a broad spectrum of eukaryotes [6], experimental studies have established that the ER membrane is physically continuous throughout the cell but that a lateral diffusion barrier may exist at the bud neck and compartmentalizes the membrane into an anterior domain and a posterior domain by limiting the exchange of ER proteins between these two domains. See e.g. [1,7]. From a biological perspective, biologists have suggested that the barrier might represent a specialized lipid domain in the bud neck featuring a different composition from the rest of the ER membrane.

[0]**Abbreviations:** PDE, partial differential equation; ER, endoplasmic reticulum; FLIP, Fluorescence Loss in Photobleaching

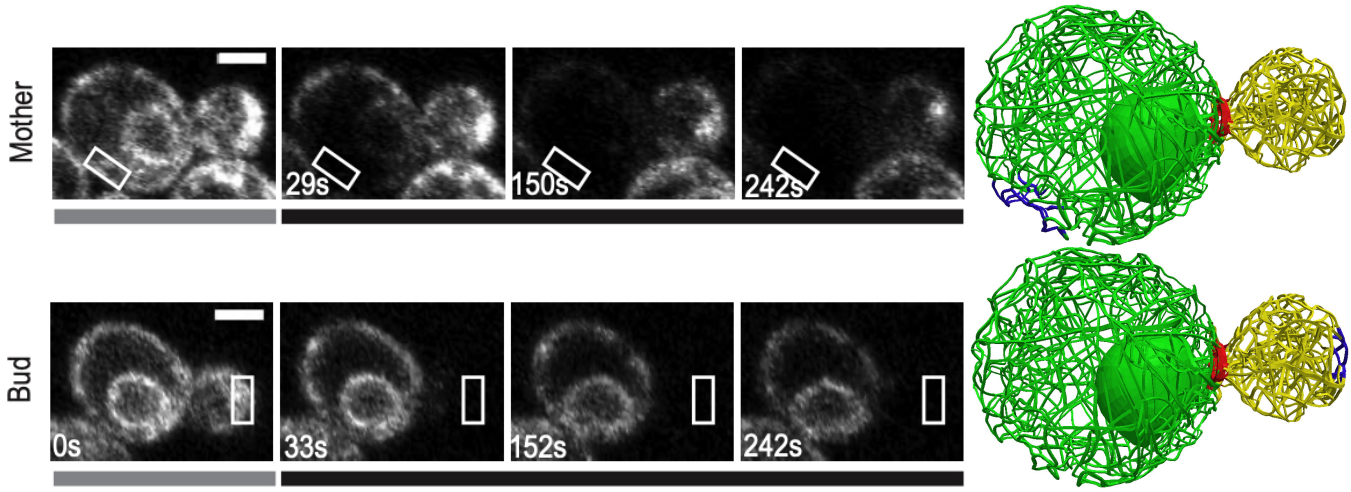

Figure 1 Confocal images of FLIP experiments in the mother (top) or bud (bottom) expressing the membrane marker Sec61-GFP. Gray bars indicate the first pre-bleached images, while black bars indicate snapshots at specific instants of repeated bleaching in the remainder of the experiment. Photobleached areas indicated by white rectangles. (Right) Segmented geometries showing: Γ_m (green), Γ_b (yellow), Γ_r (red), and the photobleached areas $\Gamma_1 \in \Gamma_m$ (top, blue) or $\Gamma_2 \in \Gamma_b$ (bottom, blue).

Studying the mobility of fluorescently tagged molecules in the ER membrane can provide biologists with important insights into the cellular function and organization. The Fluorescence Loss In Photobleaching technique, referred to as FLIP, is used in the laboratory to measure the mobility and molecular dynamics of proteins in living cells. It consists of repeatedly exposing mobile fluorescent molecules in a defined area to an intense light pulse over time by a high-intensity laser beam, thus inducing irreversible photochemical bleaching of this area, see[8,4]. Due to molecular mobility, a fairly uniform decrease in fluorescence signal is observed over time throughout the membrane and is proportional to ER protein concentration; Areas disconnected from the photobleached area should however continue to fluoresce. The rate at which fluorescence intensity changes after bleaching can provide experimenters with information about the movement of bleached molecules and the surface diffusion properties in a particular region of a living cell. We notice that the amount of fluorescence measured after bleaching in each cell compartment is always normalized to the amount before bleaching.

Intriguingly, several experimental studies have shown that the kinetics of membrane proteins are very slow between the mother and bud compartments compared to the kinetics within each region where the rates of fluorescence loss are comparable. Indeed, applying FLIP in Γ_m results in rapid depletion of fluorescence signal in Γ_m, while fluorescence is lost only slowly in Γ_b; Conversely, applying FLIP in Γ_b leads to rapid photobleaching of the marker in Γ_b but not in Γ_m[8]. Accordingly, biologists rationalize that although the ER is physically continuous, its membrane is compartmentalized, suggesting the presence of a barrier between the different domains of the ER where the diffusion of proteins in the membrane is restricted somewhere[9]; If confirmed, this theory will have a major role in maintaining and possibly optimizing the life expectancy of nascent cells. Indeed, daughter cells are born with a full life expectancy, while mothers age after each division. It has now been shown in the literature that ER stress triggers mechanisms that age yeast cells. Interestingly, compartmentalization may play a key role in retaining damage and aging factors between mothers and renewing cells by preventing the stresses that cause aging from entering the daughter cells[10,11,6]. This remains a very thorny area of research where several elements remain unclear. To date, it remains challenging to prove and elucidate the biological relevance of such barriers. To numerically study the properties of molecular diffusion and compartmentalization on the ER membrane, we first perform several FLIP experiments in the laboratory using confocal microscopy[8]. In each FLIP experiment, we collected pointwise measurement data of the total amount of fluorescence separately in each cell compartment after photobleaching and at specific time points. These data will be used in the mathematical modeling framework detailed thereafter.

Numerical simulation tools based on mathematical modeling using optimal control have the potential to further investigate the aforementioned empirical diffusion barrier theory. The optimal control problems governed by convection or convection-diffusion equations play an important role in many biomedical and engineering applications, see e.g[12,13,14,15,16,17,18,19,20]. Data assimilation formalism represents an appropriate framework for estimating model parameters, where the problem should be

formulated as a PDE constrained optimization so that the key parameters maximize a performance criterion subject to an appropriate set of constraints. We shall minimize a cost functional measuring the discrepancy between the numerical solutions and the data measurements, while the model parameters represent the control variables that allow the observations to be "better approximated" in some sense[21,22]. The first-order necessary conditions for optimality, called Karush-Kuhn-Tucker conditions, enable to derive an optimality system composed by "the state problem", "the adjoint problem" and "the inversion equations". In the existing literature, Lagrange finite element discretizations of optimal control problems have been widely used in numerical approximations of such problems. There have been several theoretical analyzes and contributions to numerical strategies and algorithms for various applications of optimal control, see e.g[23,24,25,26,27,28,29,30,31,14,32]. Moreover, an extensive literature on the topic of numerical methods for the optimal control of PDE can be found in[33,34,35].

The aim of this paper is to present a numerical method for estimating the model parameters using the optimal control theory and to explore the barrier theory, without approaching the theoretical aspects of the problem. This is part of a larger ongoing work to understand the kinetics of ER proteins in different biological cells, while considering in the future both more accurate mathematical models and the uncertainty quantification in solution. The outline of this article is as follows. We introduce in section 2 the mathematical model and the optimal control formulation for the current biological problem. In the section 3, we present the numerical method and the iterative algorithm implemented. Section 4 is devoted to the results of some numerical experiments, and to the numerical exploration of the diffusion barrier theory.

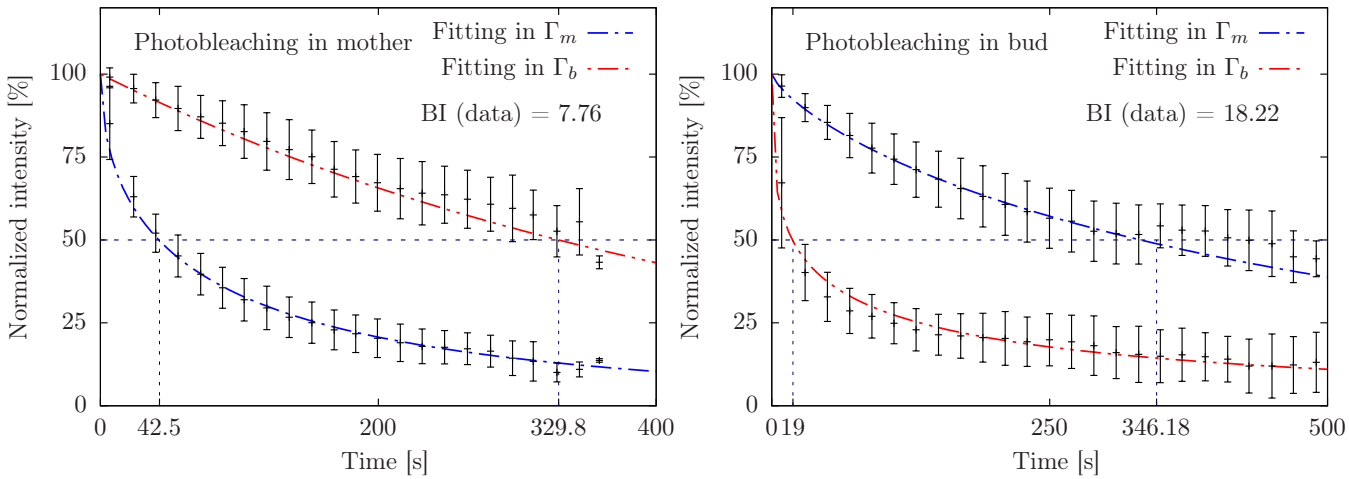

Figure 2 Experimental data showing the fluorescence signal decay over time in mother and bud compartments after an average of twenty FLIP experiments. Photobleaching is applied to Γ_1 (left) and Γ_2 (right). Original fluorescence intensity before bleaching is set to 100% in each compartment. Mean ± SD.

2 | MATHEMATICAL SETTING

In this section, we describe the mathematical setting for the data-driven model describing the dynamics of fluorescently labeled molecules on the yeast ER membrane. The acquisition of experimental data is briefly described.

2.1 | Data acquisition

We proceed with a series of FLIP experiments in budding yeast using time-lapse laser-scanning confocal microscopy expressing the ER membrane marker Sec61-GFP. All experiments were done at room temperature of 23 degrees Celsius.

The FLIP experiments were performed as described in the previous study[8] with some changes as shown in the following. The cells were imaged on LSM 780 confocal microscope (Carl Zeiss, Jena, Germany) confocal microscope. The ZEN 2011 software (Carl Zeiss) was used to control the microscope. Bleaching was applied with 100 iterations at a laser power of 100%.

All cells were pooled and transferred to Prism 6.05 (GraphPad Software, La Jolla, California), in which a one-phase decay curve constraining the first bleaching point to 100% was fitted. All intensity values were normalized against the total cell intensity and set to the value of 100% at the start of each experiment. In each FLIP experiment, we collected pointwise measurement data of the total amount of fluorescence separately in each cell compartment after photobleaching and at specific time points. Mean and standard deviations (SD) values were calculated from replicated experiments. Fig 1 (left) shows a budding yeast cell expressing the marker GFP-HDEL through serial optical sections, in which images were processed using the software ImageJ 1.49g (National Institutes of Health).

To investigate the diffusion barrier theory, measurements of the fluorescence signal from two series of FLIP experiments were collected. In the first series of experiments, photobleaching is applied in the mother cortex on $\Gamma_1 \subset \Gamma_m$, while it is applied to the bud compartment on $\Gamma_2 \subset \Gamma_b$ in the second series of experiments, see Fig 1. Fig 2 reports the decay the amount of fluorescence signal over time in the two membrane compartments. Each experiment was repeated an average of twenty times and error bars indicate the standard deviations (SD) in the collected data.

For the numerical computations, a realistic geometry of the ER membrane, referred to as Γ, is segmented based on serial optical sections through a yeast cell. Let $\mathcal{T}_h$ be partition of Γ consisting of geometrically conforming open simplicial elements K (triangles), such that $\overline{\Gamma} = \bigcup_{K \in \mathcal{T}_h}$. Several mesh tools are used to build, improve mesh quality and avoid badly stretched mesh elements K. The initially segmented surface mesh in `STL` format is locally repaired and smoothed using MeshLab[1] and the modules for mesh optimization in Netfabb[2]. We also rely on Autodesk Maya[3] for mesh quality improvement. The unstructured triangular mesh is finally remeshed and optimized using the `Frontal` algorithm of Gmsh[4], see further details in [36,37]. We evaluate the mesh quality as the ratio of the longest edge to the shortest edge of each mesh element K. In particular, the built mesh depicted in Fig 1 has $110'760$ triangles, with an element edges ratio larger than 0.3 for all elements.

2.2 | Direct problem

The timescale of a FLIP experiment is minutes, so that the most relevant dynamic process is fluorescence drain due to photobleaching. In addition, we assume, as in so many biological situations, that the fluorescently tagged molecules are free. Consequently, we suppose that the FLIP recovery of the reporter protein reflects a time-resolved pure surface diffusion dominant scenario.

Consider a sufficiently smooth, orientable and closed surface $\Gamma \subset \mathbb{R}^3$, with an outward facing normal $\mathbf{n}$. Let $(0,T)$ be a specified time interval corresponding to the period of the experiment and denote $\Gamma_T := (0,T) \times \Gamma$ for $i \in \{1,2\}$. We introduce u_1 and u_2 as protein concentrations on the ER membrane at time $t \in (0,T)$ for the aforementioned series of FLIP experiments, i.e. when photobleaching is applied to G_1 and Γ_2, respectively.

The model contains parameters of unknown value which will be identified by means of optimal control. Therefore, we introduce the set of control variables μ_m , μ_b and μ_r which respectively represent the diffusion parameters of the reporter protein in the mother, the bud and the bud neck area. We denote by χ_i the characteristic function which serves as an indicator of the surface Γ_i, with $i \in \{1,2,m,r,b\}$. The total diffusion is then given by $\mu_{tot} = \mu_m \chi_m + \mu_b \chi_b + \mu_r \chi_r$.

Essential boundary conditions must be prescribed on $\partial\Gamma_1$ in the first set of experiments and on $\partial\Gamma_2$ when photobleaching is applied to the bud. To allow the use of the same finite element mesh in both sets of FLIP experiments and avoid further mesh manipulations on the boundaries, we consider a penalty method such as a penalty parameter $1/\varepsilon$ helps maintain zero concentration in bleached areas, see e.g. [38,39,37,40] for other applications of penalty methods. The adjustment of the penalty parameter can be problematic in certain problems because a too large penalty parameter can deteriorate the conditioning of the resulting linear system and induce instabilities, see for example [36].

In addition, we assume pointwise bounds on the key parameters to avoid non-physical values during optimization iterations. We consider the admissible set of parameters

$$\mathcal{U}_{ad} = \left\{ \left(\mu_m, \mu_b, \mu_r\right) \in \mathbb{R}^3 \,:\, 0 < \mu_m \leqslant A,\ 0 < \mu_b \leqslant B,\ 0 < \mu_r \leqslant C \right\},$$

where A, B and C are fixed values. Let $\mathbf{I}$ represent the identity tensor. For an arbitrary function ϕ and vector $\mathbf{v}$ in suitable function spaces, we introduce the surface gradient, the surface divergence and the Laplace-Beltrami operators as follows:

[1] MeshLab - http://meshlab.sourceforge.net
[2] Netfabb - http://www.netfabb.com
[3] Maya - http://www.autodesk.com/products/maya
[4] Gmsh - http://www.geuz.org/gmsh

$$\begin{aligned}\boldsymbol{\nabla}_\Gamma \phi &= (\mathbf{I}-\mathbf{n}\otimes\mathbf{n})\boldsymbol{\nabla}\phi \;= \boldsymbol{\nabla}\phi - (\mathbf{n}.\boldsymbol{\nabla}\phi)\,\mathbf{n},\\ \mathrm{div}_\Gamma \mathbf{v} &= (\mathbf{I}-\mathbf{n}\otimes\mathbf{n}) : \boldsymbol{\nabla}\mathbf{v} = \mathrm{div}\,\mathbf{v} - ((\boldsymbol{\nabla}\mathbf{v})\,\mathbf{n}).\mathbf{n},\\ \Delta_\Gamma \phi &= \mathrm{div}_\Gamma\left(\boldsymbol{\nabla}_\Gamma\phi\right),\end{aligned}$$

where the tensorial product of two vectors is denoted $\otimes$, and the two times contracted product between tensors is denoted by the semicolon. They correspond to the two-dimensional operators evaluated in the tangent plane to the ER membrane Γ. The projector tensor $\mathbf{I}-\mathbf{n}\otimes\mathbf{n}$ has zero eigenvalue, that is $(\mathbf{I}-\mathbf{n}\otimes\mathbf{n})\,\mathbf{n}=\mathbf{0}$, leading to non-diffusion in the direction normal to the surface. Equipped with initial conditions $u_{1,0}$ and $u_{2,0}$, the forward problem reads

SP(u_1,u_2) : For given μ_m, μ_b, μ_r belonging to $\mathcal{U}_{ad}$, find u_1 and u_2 satisfying

$$\frac{\partial u_1}{dt} - \mathrm{div}_\Gamma\left(\left(\mu_m\chi_m+\mu_b\chi_b+\mu_r\chi_r\right)\boldsymbol{\nabla}_\Gamma u_1\right) + \frac{1}{\varepsilon}u_1\chi_1 = 0 \qquad \text{in } (0,T)\times\Gamma, \tag{2.1}$$

$$\frac{\partial u_2}{dt} - \mathrm{div}_\Gamma\left(\left(\mu_m\chi_m+\mu_b\chi_b+\mu_r\chi_r\right)\boldsymbol{\nabla}_\Gamma u_2\right) + \frac{1}{\varepsilon}u_2\chi_2 = 0 \qquad \text{in } (0,T)\times\Gamma, \tag{2.2}$$

$$u_1(t=0,\cdot) = u_{1,0}(\cdot) \qquad \text{in } \Gamma, \tag{2.3}$$

$$u_2(t=0,\cdot) = u_{2,0}(\cdot) \qquad \text{in } \Gamma. \tag{2.4}$$

We use the so-called *optimize then discretize* approach rather than the *discretize then optimize* approach, ie the optimality conditions are derived and then discretized after writing the variational formulation.

2.3 | Inverse problem and parameter identification

The experimental framework of FLIP provides measurements of fluorescence loss kinetics in each cell cortex at discrete time points over the interval $(0,T)$, so that the average protein concentration in each compartment is normalized to the concentration before the bleaching process. However, the spatio-temporal evolution of the fluorescence decay cannot be provided by the experimental setting. We first proceed with a nonlinear least-squares curve fitting of the experimental data of the total amount of fluorescence over time, as depicted in Fig. 2. Indeed, let $F_{m,1}(.)$ and $F_{b,1}(.)$ be the time evolution functions of fluorescence loss in Γ_m and Γ_b, respectively, obtained by fitting after averaging twenty FLIP experiments in which photobleaching is applied to the mother at Γ_1. Similarly, $F_{m,2}(\cdot)$ and $F_{b,2}(\cdot)$ denote the time evolution functions of fluorescence decay in Γ_m and Γ_b, respectively, obtained by fitting after averaging twenty FLIP experiments in which photobleaching is applied at Γ_2.

The inverse problem consists in finding the optimal parameters $\mu_m^\star$, $\mu_b^\star$, and $\mu_r^\star$ such that the averaging solutions of the direct problem SP$(u_1^\star,u_2^\star)$ match as closely as possible the target averaging concentrations in each compartment. For $t\in(0,T)$, $l\in\{m,b\}$ and $i\in\{1,2\}$, and given the curve fitting functions $F_{l,i}(t)$, the optimization problem is formulated as:

$$\begin{aligned}&\text{Find optimal parameters } \left(\mu_m^\star,\mu_b^\star,\mu_r^\star\right) = \underset{\mu_{j\in\{m,b,r\}}\in\mathcal{U}_{ad}}{\arg\inf}\ \mathcal{J}\left(u_1,u_2\,;\,\mu_m,\mu_b,\mu_r\right),\\ &\qquad\text{subject to the forward problem SP (2.1-2.4) as a constraint.}\end{aligned} \tag{2.5}$$

The cost functional $\mathcal{J}$ is constructed by matching the temporal evolution of the average concentration predicted by the model in each cell compartment with the corresponding target experimental measurements. It depends on both the state variables and the controls and is expressed as:

$$\begin{aligned}\mathcal{J}\left(u_1,u_2;\mu_m,\mu_b,\mu_r\right) = &\sum_{i=1,2}\frac{\alpha_{m,i}}{2}\Big(\int_0^T\int_{\Gamma_m} u_i - \int_0^T F_{m,i}(t)\int_{\Gamma_m}u_{1,0}\Big)^2 + \frac{\alpha_{b,i}}{2}\Big(\int_0^T\int_{\Gamma_b} u_i - \int_0^T F_{b,i}(t)\int_{\Gamma_b}u_{2,0}\Big)^2\\ &+\sum_{i=1,2}\frac{\gamma_{m,i}}{2}\Big(\int_{\Gamma_m} u_i(T,\cdot) - F_{m,i}(T)\int_{\Gamma_m}u_{1,0}\Big)^2 + \frac{\gamma_{b,i}}{2}\Big(\int_{\Gamma_b} u_i - F_{b,i}(T)\int_{\Gamma_b}u_{2,0}\Big)^2\\ &+\frac{\delta}{2}\left|\mu_m-\mu_b\right|^2 + \sum_{j\in\{m,b,r\}}\frac{\delta_j}{2}\mu_j^2.\end{aligned} \tag{2.6}$$

The terms weighted by $\alpha_{l,i}$, with $l \in \{m, b\}$ and $i \in \{1, 2\}$, measure the mismatch between the numerical solution and targets throughout the time interval $(0, T)$, whereas the terms weighted by $\gamma_{l,i}$, with $l \in \{m, b\}$ and $i \in \{1, 2\}$, measure this discrepancy at fixed time $t = T$. The latter corresponds to an optimal control with desired states only at the final instant. An appropriate choice of these weights, possibly zero, allows more emphasis to be placed on the solutions matching the targets throughout the duration of the experiment or at the end time; The latter can be replaced by any particular time in $(0, T)$. The δ-weighted term helps account for the expectation of biologists that similar protein diffusion rates are expected in the mother and bud compartments. Finally, the terms weighted with δ_j, with $j \in \{m, b, r\}$, are the so called Tykhonov regularization used to circumvent the possibly ill-posed character of the inverse problem and thwart the tendency of controls to become locally unlimited[41,42]. A more in-depth discussion on the choice of the regularization parameter is available in[43] but is outside the scope of this work. Remark that the weights in the objective functional helps to put more emphasis on some components with respect to the other components. In practice, we can choose either $\alpha_1 = \alpha_2 = 0$ or $\gamma_1 = \gamma_2 = 0$.

To derive the Karush-Kuhn-Tucker optimality conditions, we introduce the adjoint variables $v_1(t, \boldsymbol{x})$ and $v_2(t, \boldsymbol{x})$ of the corresponding state variables $u_1(t, \boldsymbol{x})$ and $u_2(t, \boldsymbol{x})$, respectively. The associated Lagrangian functional is expressed by

$$\begin{aligned}\mathcal{L}\left(u_{i\in\{1,2\}}; v_{i\in\{1,2\}}; \mu_{j\in\{m,b,r\}}\right) = \; & \mathcal{J}\left(u_{i\in\{1,2\}}; \mu_{j\in\{m,b,r\}}\right) \\ & - \sum_{i\in\{1,2\}} \Big(\int_{\Gamma_T} \frac{\partial u_i}{dt} v_i + \int_{\Gamma_T} \left(\mu_m \chi_m + \mu_b \chi_b + \mu_r \chi_r\right) \boldsymbol{\nabla}_\Gamma u_i \cdot \boldsymbol{\nabla}_\Gamma v_i + \int_{\Gamma_T} \frac{1}{\varepsilon}\, \chi_i u_i v_i \Big). \end{aligned} \tag{2.7}$$

The first-order optimality conditions are found by imposing the stationarity of the Lagrangian functional with respect to the adjoint, state, and inversion variables, respectively. Let $D\mathscr{L}\left[\delta_\psi\right]$ be the first variation of $\mathscr{L}$ with respect to a variable ψ. The stationarity of the Lagrangian with respect to the adjoint variables $D\mathcal{L}\left[\delta_{v_1,v_2}\right] = 0$ provides the forward problem SP (2.1-2.2). The adjoint system is obtained by requiring the stationarity of the Lagrangian functional with respect to the state variables, that is $D\mathcal{L}\left[\delta_{u_1,u_2}\right] = 0$. The adjoint equations are given by:

AP $\left(v_1, v_2\right)$: Given the state variables u_1 and u_2 and the control variables $\mu_{j\in\{m,b,r\}} \in \mathcal{U}_{ad}$, find v_1 and v_2 such that

$$-\frac{\partial v_1}{dt} - \mathrm{div}_\Gamma\left(\left(\mu_m \chi_m + \mu_b \chi_b + \mu_r \chi_r\right) \boldsymbol{\nabla}_\Gamma v_1\right) + \frac{1}{\varepsilon} v_1 \chi_1 = \sum_{k=m,b} \sum_{j=1,2} \alpha_{k,j} \Big(\int_0^T \int_{\Gamma_k} u_1 - \int_0^T \int_{\Gamma_k} F_{k,j} u_{1,0} \Big) \chi_k \quad \text{in } (0,T)\times\Gamma, \tag{2.8}$$

$$-\frac{\partial v_2}{dt} - \mathrm{div}_\Gamma\left(\left(\mu_m \chi_m + \mu_b \chi_b + \mu_r \chi_r\right) \boldsymbol{\nabla}_\Gamma v_2\right) + \frac{1}{\varepsilon} v_2 \chi_2 = \sum_{k=m,b} \sum_{j=1,2} \alpha_{k,j} \Big(\int_0^T \int_{\Gamma_k} u_2 - \int_0^T \int_{\Gamma_k} F_{k,j} u_{2,0} \Big) \chi_k \quad \text{in } (0,T)\times\Gamma, \tag{2.9}$$

$$v_1(t = T, \cdot) = \sum_{k=m,b} \sum_{j=1,2} \gamma_{k,j} \Big(\int_{\Gamma_k} u_1(T, \cdot) - F_{k,j}(T) \int_{\Gamma_k} u_{1,0} \Big) \chi_k \quad \text{in } \Gamma, \tag{2.10}$$

$$v_2(t = T, \cdot) = \sum_{k=m,b} \sum_{j=1,2} \gamma_{k,j} \Big(\int_{\Gamma_k} u_2(T, \cdot) - F_{k,j}(T) \int_{\Gamma_k} u_{2,0} \Big) \chi_k \quad \text{in } \Gamma, \tag{2.11}$$

Notice that the adjoint equations (2.8) and (2.9) are solved backwards in time, which therefore requires terminal conditions (2.10) and (2.11) instead of initial conditions.

For given $a, b, x \in \mathbb{R}$, let $\pi_{[a,b]}\{x\} = \max\left(\min\left(x, b\right), a\right)$ be the projection of x on the interval $[a, b]$. By imposing the stationarity of the Lagrangian with respect to the inversion parameters, i.e. $D\mathcal{L}[\delta_{\mu_m,\mu_b,\mu_r}] = 0$, the inversion equations provide an explicit characterization of the the optimal controls as follows.

Given the state variables u_1 and u_2 and the adjoint variables v_1 and v_2, the optimal control variables read:

$$\mu_m^\star = \mathbb{m}_{[0,A]}\Big\{ \frac{\delta_b}{\delta\delta_m + \delta_b(\delta + \delta_m)} \sum_{i=1,2} \int_0^T \int_{\Gamma_m} \boldsymbol{\nabla}_\Gamma u_i \cdot \boldsymbol{\nabla}_\Gamma v_i + \frac{\delta}{\delta\delta_m + \delta_b(\delta + \delta_m)} \sum_{k=m,b} \sum_{i=1,2} \int_0^T \int_{\Gamma_k} \boldsymbol{\nabla}_\Gamma u_i \cdot \boldsymbol{\nabla}_\Gamma v_i \Big\}, \tag{2.12}$$

$$\mu_b^\star = \mathbb{m}_{[0,B]}\Big\{ \frac{\delta + \delta_m}{\delta} \mu_m^\star - \frac{1}{\delta} \sum_{i=1,2} \int_0^T \int_{\Gamma_m} \boldsymbol{\nabla}_\Gamma u_i \cdot \boldsymbol{\nabla}_\Gamma v_i \Big\}, \tag{2.13}$$

$$\mu_r^\star = \mathbb{T}_{[0,C]}\Big\{ \frac{1}{\delta_r} \sum_{i=1,2} \int_0^T \int_{\Gamma_r} \nabla_\Gamma u_i \cdot \nabla_\Gamma v_i \Big\}. \tag{2.14}$$

From a numerical point of view, we have rather opted for the use of a gradient-based optimization algorithm instead of an exact evaluation of the control parameters. This turned out to be more stable and it requires the evaluation of the Lagrangian gradient against the control variables as detailed afterwards.

3 | NUMERICAL APPROXIMATION

In this section, we describe the solution method based on a second-order time discretization and the numerical algorithm. Let us divide $[0,T]$ into $N+1$ subintervals $[t^n, t^{n+1})$, with $n = 0, \cdots, N$ of constant step Δt. For any $n \geqslant 1$, we denote by u_1^n, u_2^n, v_1^n and v_2^n the approximations of u_1, u_2, v_1 and v_2 at time step n , respectively. We apply a gradient descent algorithm with an adapted step length yielding a sequence of approximations to the optimal solutions and optimal key parameters. For each iteration $k \geqslant 0$ of the gradient method, we solve forward and inverse problems SP and AP using a fully implicit scheme.

For any $n \in [1, N+1]$ and $k > 0$, the approximations of the state unknowns $u_1^{k,n}$ and $u_2^{k,n}$ are computed by induction, using values at previous time steps. Similarly, for any $n \in [0, N]$, the adjoint unknowns $v_1^{k,n}$ and $v_2^{k,n}$ are computed by induction, using values at next time steps. For $i \in \{1,2\}$, the scheme is bootstrapped by initial conditions (2.3-2.4) $u_i^{-1} = u_i^0 = u_{i,0}$ and terminal conditions (2.10-2.11) $v_i^{N+2} = v_i^{N+1} = v_i(T)$, where u_i^{-1} and v_i^{N+2} only stand for convenient notations.

For each iteration k of the gradient method, the backward differentiation scheme of second order, referred to as BDF2, is used for the time derivative terms. For any $n \in [0, N]$ and $k > 0$, and given the control variables μ_j^k with $j \in \{m, b, r\}$, the state unknowns $u_1^{k,n+1}$ and $u_2^{k,n+1}$ are computed and the semi-discrete approximation in time of the forward problem reads

$$\int_\Gamma \frac{3u_i^{k,n+1} - 4u_i^{k,n} + u_i^{k,n-1}}{2\Delta t}\xi + \int_\Gamma \left(\mu_m^k \chi_m + \mu_b^k \chi_b + \mu_r^k \chi_r\right) \nabla_\Gamma u_i^{k,n+1} \cdot \nabla_\Gamma \xi + \int_\Gamma \frac{1}{\epsilon}\chi_i u_i^{k,n+1}\xi = 0, \qquad \forall \xi \in H^1(\Gamma).$$

The numerical solution of the adjoint problem is computed backward in time starting from the final time $t = T$. By change of variable $\tau \equiv T - t \in (0,T)$, we obtain $\dfrac{\partial}{\partial \tau} = -\dfrac{\partial}{\partial t}$ and the terminal condition becomes an initial condition. A similar numerical scheme is used in the semi-discrete time approximation of the adjoint system. For any $n \in [1, N+1]$ and given $u_1^{k,m}$, $u_2^{k,m}$, μ_m^k, μ_b^k and μ_r^k, with $m \in [1, N+1]$, the semi-discrete adjoint problem consists in finding $v_1^{k,n-1}$ and $v_2^{k,n-1}$ such that

$$\int_\Gamma \frac{3v_i^{k,n-1} - 4v_i^{k,n} + v_i^{k,n+1}}{2\Delta t}\xi + \int_\Gamma \left(\mu_m^k \chi_m + \mu_b^k \chi_b + \mu_r^k \chi_r\right) \nabla_\Gamma v_i^{k,n-1} \cdot \nabla_\Gamma \xi + \int_\Gamma \frac{1}{\epsilon}\chi_i v_i^{k,n-1}\xi =$$

$$\sum_{l=m,b} \sum_{j=1,2} \alpha_{l,j} \left(\int_0^T \int_{\Gamma_l} u_i^k - \int_0^T \int_{\Gamma_l} F_{l,j} u_{i,0} \right) \chi_l \xi, \qquad \forall \xi \in H^1(\Gamma).$$

Regarding the finite element space discretization, a high-order finite element approximation using $\mathbb{P}_\kappa(K)$, with $\kappa \geqslant 1$ and $K \in \mathcal{T}_h$ is used for the state and adjoint variables .

At the computational level, some stability issues are encountered when using an exact evaluation of the optimal controls (2.12-2.13-2.14) at each optimization iteration. Therefore, we have rather used a gradient-based optimization algorithm. That requires the evaluation of the gradient of the Lagrangian with respect to the control variables. Provided with an initial guess for the controls μ_m^0, μ_b^0, and μ_r^0 and a starting value for the descent length, the control variables are updated along the gradient direction using an adapted step length λ^k as follows (3.1-3.2-3.3).

GU $\left(\mu_m^k, \mu_b^k, \mu_r^k\right)$: For $k > 0$, given $\left(u_i^{k-1}, v_i^{k-1}\right)$ with $i \in \{1,2\}$ and μ_j^{k-1} with $j \in \{m, b, r\}$, compute:

$$\mu_m^k = \mathbb{T}_{[0,A]}\left\{ \mu_m^{k-1} - \lambda^k \left(\delta_m \mu_m^{k-1} + \delta\left(\mu_m^{k-1} - \mu_b^{k-1}\right) - \sum_{i=1,2} \int_0^T \int_{\Gamma_m} \nabla_\Gamma u_i^{k-1} \cdot \nabla_\Gamma v_i^{k-1} \right) \right\}, \tag{3.1}$$

$$\mu_b^k = \mathbb{m}_{[0,B]}\left\{ \mu_b^{k-1} - \lambda^k \left(\delta_b \mu_b^{k-1} + \delta \left(\mu_b^{k-1} - \mu_m^{k-1} \right) - \sum_{i=1,2} \int_0^T \int_{\Gamma_b} \nabla_\Gamma u_i^{k-1} \cdot \nabla_\Gamma v_i^{k-1} \right) \right\}, \tag{3.2}$$

$$\mu_r^k = \mathbb{m}_{[0,C]}\left\{ \mu_r^{k-1} - \lambda^k \left(\delta_r \mu_r^{k-1} - \sum_{i=1,2} \int_0^T \int_{\Gamma_r} \nabla_\Gamma u_i^{k-1} \cdot \nabla_\Gamma v_i^{k-1} \right) \right\}. \tag{3.3}$$

We proceed with an adaptation strategy for the step length λ^k to ensure the decrease of the cost functional. Indeed, the step length is rejected and therefore decreased in the case where the cost functional does not decrease. Control variables are only updated if the step length is accepted, while we exit the algorithm if λ drops below a threshold value ϵ_λ. The gradient descent iterations are repeated until the relative change in the cost functional becomes smaller than a given tolerance $\epsilon_{\mathcal{J}}$. Convergence is achieved at iteration $k > 0$ if

$$err \equiv \frac{\left| \mathcal{J}^k - \mathcal{J}^{k-1} \right|}{\left| \mathcal{J}^{k-1} \right|} < \epsilon_{\mathcal{J}}, \qquad \text{with } \mathcal{J}^k \equiv \mathcal{J}\left(u^k_{i\in\{1,2\}}; \mu^k_{j\in\{m,b,r\}} \right).$$

The pseudo-code of the overall iterative scheme is detailed in Algorithm 1.

Algorithm 1 Strategy of the optimal control problem

Set $k \leftarrow 0$, $err \leftarrow 2\epsilon_{\mathcal{J}}$
Let $(u_{1,0}, u_{2,0})$ be the known initial condition, and $\left(\mu_m^0, \mu_b^0, \mu_r^0\right)$ be the initial guess
for $n = 0, \cdots, N \equiv \dfrac{T}{\Delta t}$ **do**
    Solve SP $\left(u_1^{0,n+1}, u_2^{0,n+1}\right)$ with $u_i^{0,0} = u_{i,0}$ (initialization)
end for
Evaluate $\mathcal{J}^0$
while $err \geqslant \epsilon_{\mathcal{J}}$ **do**
    $\lambda \leftarrow 6\lambda/5$
    for $n = N+1, \cdots, 1$ **do**
        Solve AP $\left(v_1^{k,n-1}, v_2^{k,n-1}\right)$ using $u_1^{k,N+1}$ and $u_2^{k,N+1}$ for terminal conditions
    end for
    $k \leftarrow k+1$
    Compute GU $\left(\mu_m^k, \mu_b^k, \mu_r^k\right)$
    for $n = 0, \cdots, N$ **do**
        Solve SP $\left(u_1^{k,n+1}, u_2^{k,n+1}\right)$ with $u_i^{k,0} = u_{i,0}$
    end for
    Evaluate $\mathcal{J}\left(u^k_{i\in\{1,2\}}; \mu^k_{j\in\{m,b,r\}}\right)$
    while $\mathcal{J}^k > \mathcal{J}^{k-1}$ **do**
        $\lambda \leftarrow 3\lambda/4$
        if $\lambda < \epsilon_\lambda$ **then return** "Algorithm stagnated"
        end if
        Re-compute GU $\left(\mu_m^k, \mu_b^k, \mu_r^k\right)$
        for $n = 0, \cdots, N$ **do**
            Re-solve SP $\left(u_1^{k,n+1}, u_2^{k,n+1}\right)$ with $u_i^{k,0} = u_{i,0}$
        end for
        Re-evaluate $\mathcal{J}\left(u^k_{i\in\{1,2\}}; \mu^k_{j\in\{m,b,r\}}\right)$
    end while
    $err \leftarrow \dfrac{|\mathcal{J}^k - \mathcal{J}^{k-1}|}{|\mathcal{J}^{k-1}|}$
end while

4 | NUMERICAL RESULTS

In what follows, we provide a set of numerical examples to test the performance of the finite element method described above, with the ultimate goal of investigating numerically the barrier index theory.

The method has been implemented using the free software Rheolef[44], which represents a general purpose C++ library for scientific computing with special emphasis on finite elements and parallel computing. The parallelism relies upon MPI[5], while MUMPS is used for factorization and as direct solver on distributed-memory architectures. It relies also on the Boost[6], Blas[7], Scotch[8], and UMFPACK[9] libraries for much of its functionalities. Results are displayed graphically using Paraview[10] and Gnuplot[11]. The computations are performed on a workstation with an Intel ® Core ™ i7-4790 (3.6 GHz) processor.

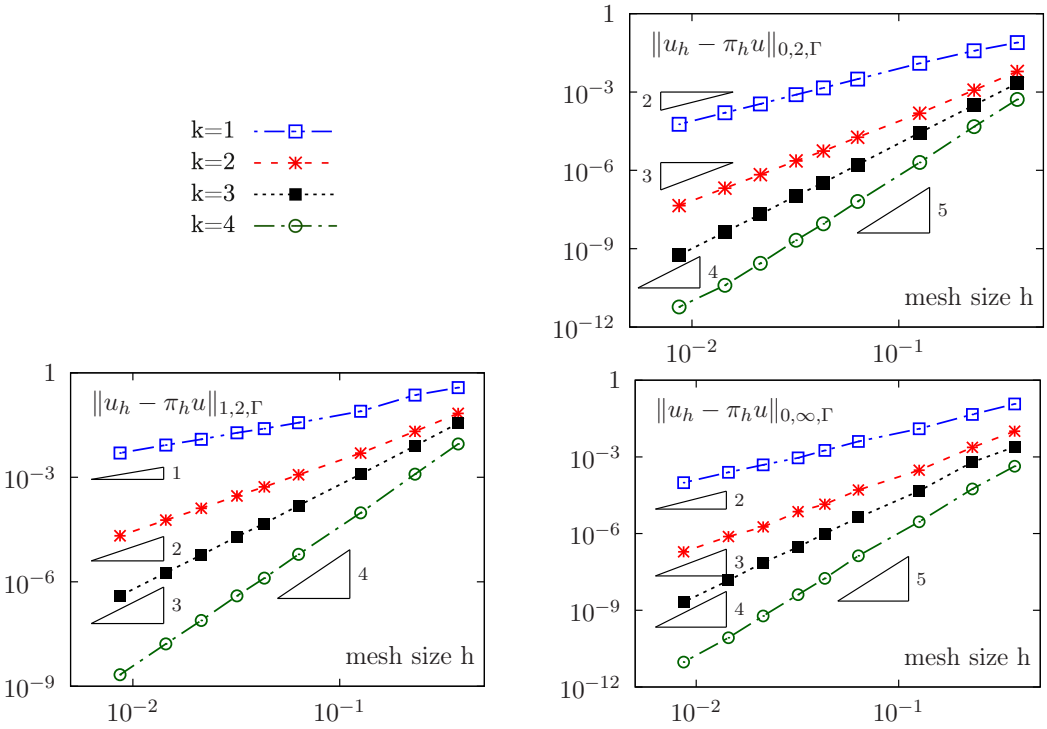

Figure 3 Example 1: Convergence study in the norms $L^2(\Gamma)$ (Top), $H^1(\Gamma)$ (Bottom left) and $L^\infty(\Gamma)$ (Bottom right) for high-order polynomial approximations $\mathbb{P}_\kappa$ and high-order curved surface meshes. The logarithmic scale is used.

4.1 | Example 1

The purpose of this example is to validate the resolution of the direct problem, mainly the assembly of surface operators for the numerical solutions of elliptic surface partial differential equations. We consider a test case presented in[45] and investigate numerically the convergence properties of the solution. The problem consists in solving:

$$u - \Delta_\Gamma u = \alpha\left(3x^2y - y^3\right) \quad \text{in } \Gamma, \qquad \text{with } \alpha = -\frac{13}{8}\sqrt{\frac{35}{\pi}}.$$

[5] Message Passing Interface - http://www.mpich.org
[6] Boost libraries - http://www.boost.org
[7] Basic Linear Algebra Subprograms library - http://www.netlib.org/blas
[8] Scotch - http://www.labri.fr/perso/pelegrin/scotch
[9] Umfpack routines - http://www.cise.ufl.edu/research/sparse/umfpack/
[10] Paraview - http://www.paraview.org
[11] Gnuplot - http://www.gnuplot.info

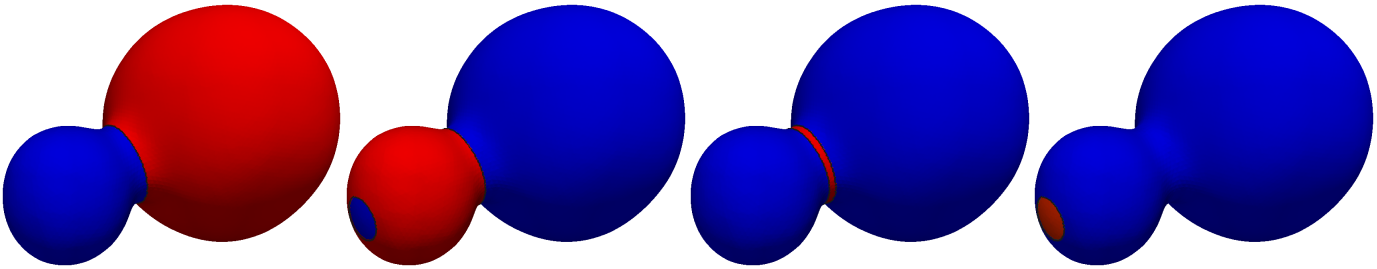

Figure 4 Example 2: Idealized and simplified geometry of yeast ER highlighting in red the mother, bud, bud neck and photobleaching areas, respectively.

The geometry is the unit sphere $\left\{\boldsymbol{x} \in \mathbb{R}^3 \,:\, |\boldsymbol{x}| = 1\right\}$ and the exact solution is given by:

$$u(\boldsymbol{x}) = \alpha \frac{|\boldsymbol{x}|^2}{12 + |\boldsymbol{x}|^2} \left(3x^2 y - y^3\right).$$

We study the spatial accuracy for high-order finite element approximations by computing the error in the norms $L^2(\Gamma)$, $H^1(\Gamma)$ and $L^\infty(\Gamma)$ of the computed solution u_h on successively refined meshes with respect to the reference exact solution $\pi_h u$, where π_h is the Lagrange interpolation operator in the corresponding finite element space.

The decrease in errors with respect to mesh size and convergence rates are shown in Fig. 3. Results depict the conformity between numerical and exact solutions for several polynomial finite element approximations. For example, for $\mathbb{P}_3$ Lagrange finite elements, the experimental order of convergence is 4 in the $L^2(\Gamma)$ norm, whereas it is equal to 3 in the $H^1(\Gamma)$ norm. The results matches the theoretical error estimates $\left\|u_h - \pi_h u\right\|_{0,2,\Gamma} < Ch^{\kappa+1}$ and $\left\|u_h - \pi_h u\right\|_{1,2,\Gamma} < Ch^{\kappa}$, where C represents a constant, $h = \max_{K \in \mathcal{T}_h} \text{diameter}(K)$ represents the mesh size, and κ is the degree of the polynomial approximation with $\kappa \in \{1, 2, 3, 4\}$, see [45].

4.2 | Example 2: Optimal control simulations in simplified geometry

In this example, we perform a numerical validation of the proposed method in the case of simplified geometry and data. To that end, we consider an idealized geometry encompassing the convex envelopes of the mother and bud cortex, and we generate successively refined semi-regular meshes. We assume that photobleaching is only applied to the bud domain and consider the

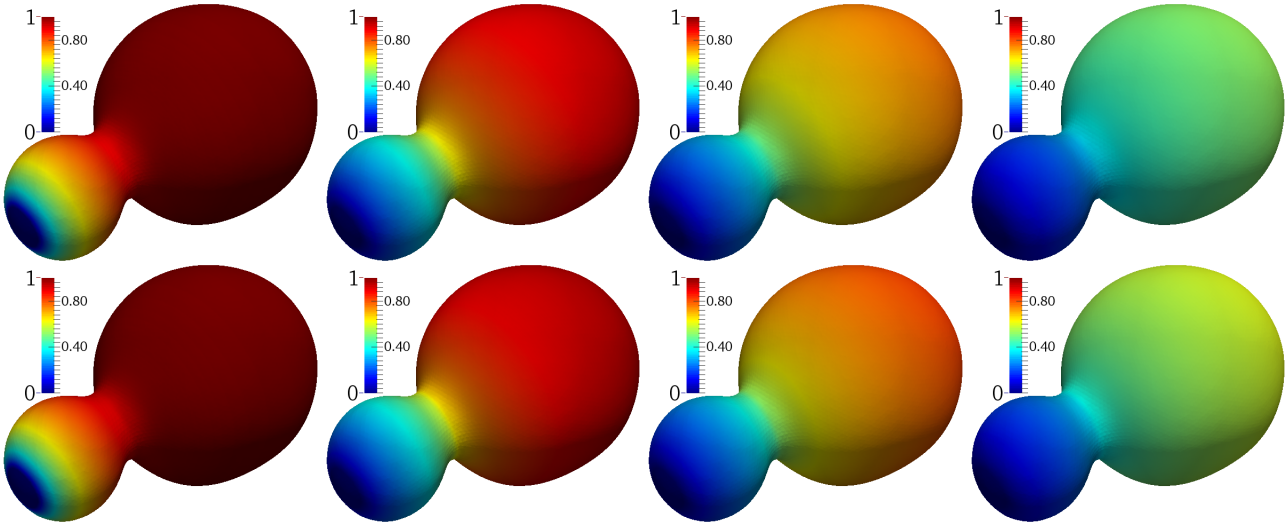

Figure 5 Example 2: Snapshots showing the computed fluorescence loss kinetics at optimal state for times $t \in \{10, 70, 170, 340\}$ with a mesh $h = 4 \times 10^{-3}$. Top: $\alpha_{m,2} = \alpha_{b,2} = 2 \times 10^4$, $\gamma_{m,2} = \gamma_{b,2} = 0$. Bottom: $\alpha_{m,2} = \alpha_{b,2} = 0$, $\gamma_{m,2} = \gamma_{b,2} = 10^8$.

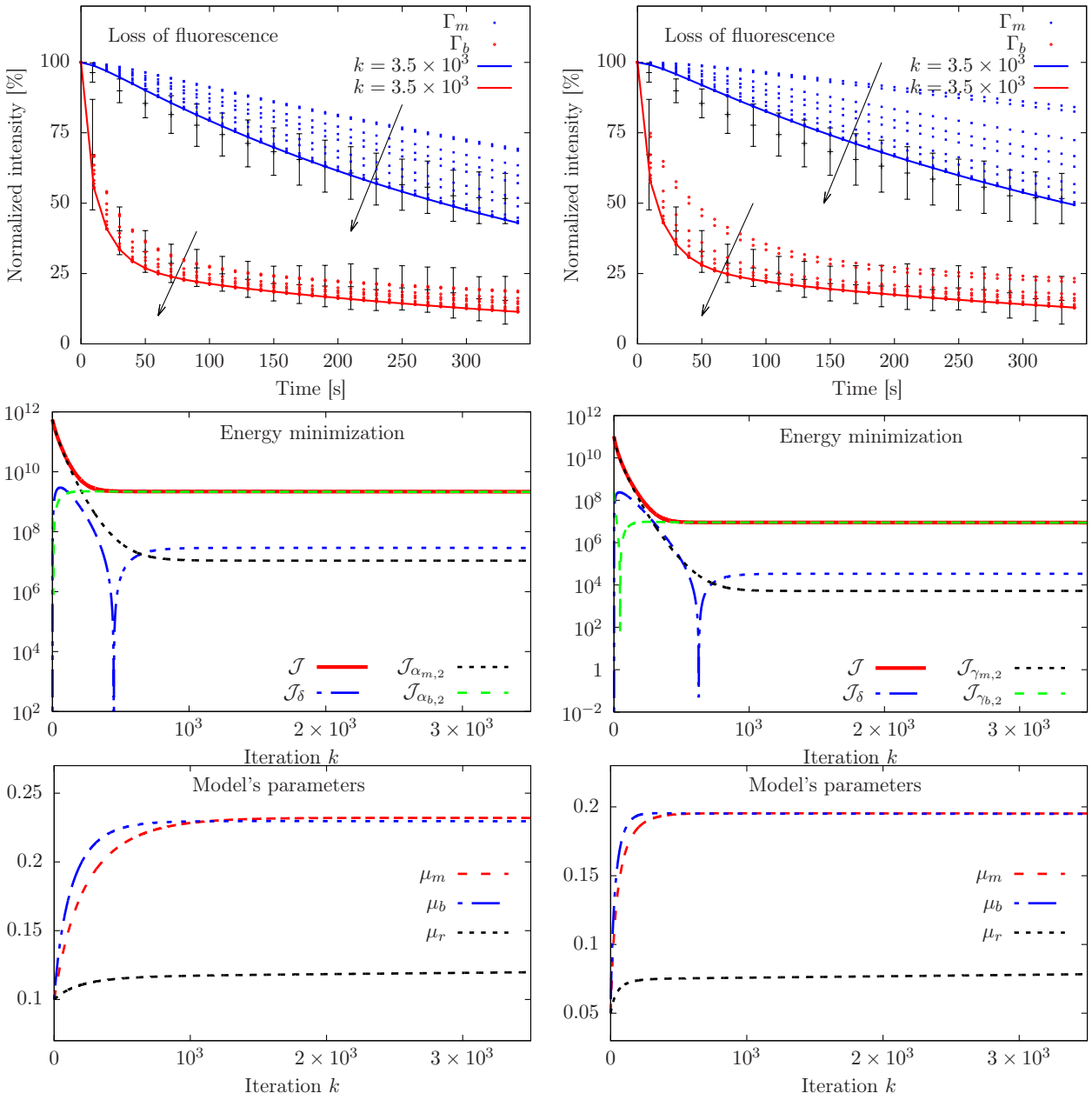

Figure 6 Example 2: Numerical results of the optimal control with the desired states enforced over the entire time period (Left: $\gamma_{m,2} = \gamma_{b,2} = 0$) and with the desired states at the final time T (Right: $\alpha_{m,2} = \alpha_{b,2} = 0$). Top: loss of fluorescence over time at particular iterations k. Center: minimization of the functional cost. Bottom: convergence of key model parameters.

corresponding experimental measurements of fluorescence loss. We define the different subdomains as shown in Fig. 4. Hence, the forward problem consists in finding u_2 satisfying (2.2-2.4), with $\alpha_{m,1} = \alpha_{b,1} = \gamma_{m,1} = \gamma_{b,1} = 0$ in (2.6).

To test the robustness of the algorithm and study the different choices of the energy to be minimized, we consider two different sets of parameters, so that we minimize the difference between the solution and the targets either over the entire time interval or at the final instant, respectively. In the first experiment, we consider $h = 0.043$, $\varepsilon = 10^{-10}$, $\mathbb{P}_1$ Lagrange polynomials, $\alpha_{m,2} = \alpha_{b,2} = 2 \times 10^4$, $\gamma_{m,2} = \gamma_{b,2} = 0$, $\delta = 10^{13}$, $\delta_m = \delta_b = \delta_r = 1$, and $\mu_m^0 = \mu_b^0 = \mu_r^0 = 0.1$. For the optimal control with desired states at the final time, we choose $h = 0.043$, $\varepsilon = 10^{-10}$, $\mathbb{P}_1$ Lagrange polynomials, $\alpha_{m,2} = \alpha_{b,2} = 0$, $\gamma_{m,2} = \gamma_{b,2} = 10^8$, $\delta = 10^{12}$, $\delta_m = \delta_b = \delta_r = 1$, and $\mu_m^0 = \mu_b^0 = \mu_r^0 = 0.05$. We run the optimal control algorithm for $t \in (0, T = 349)$ until convergence is reached. The time evolution of fluorescence loss kinetics is displayed in Fig. 6 (top) for several values of the iteration k, showing slightly different kinetics as we enforce the matching with the data in different ways. In Fig. 6 (top right),

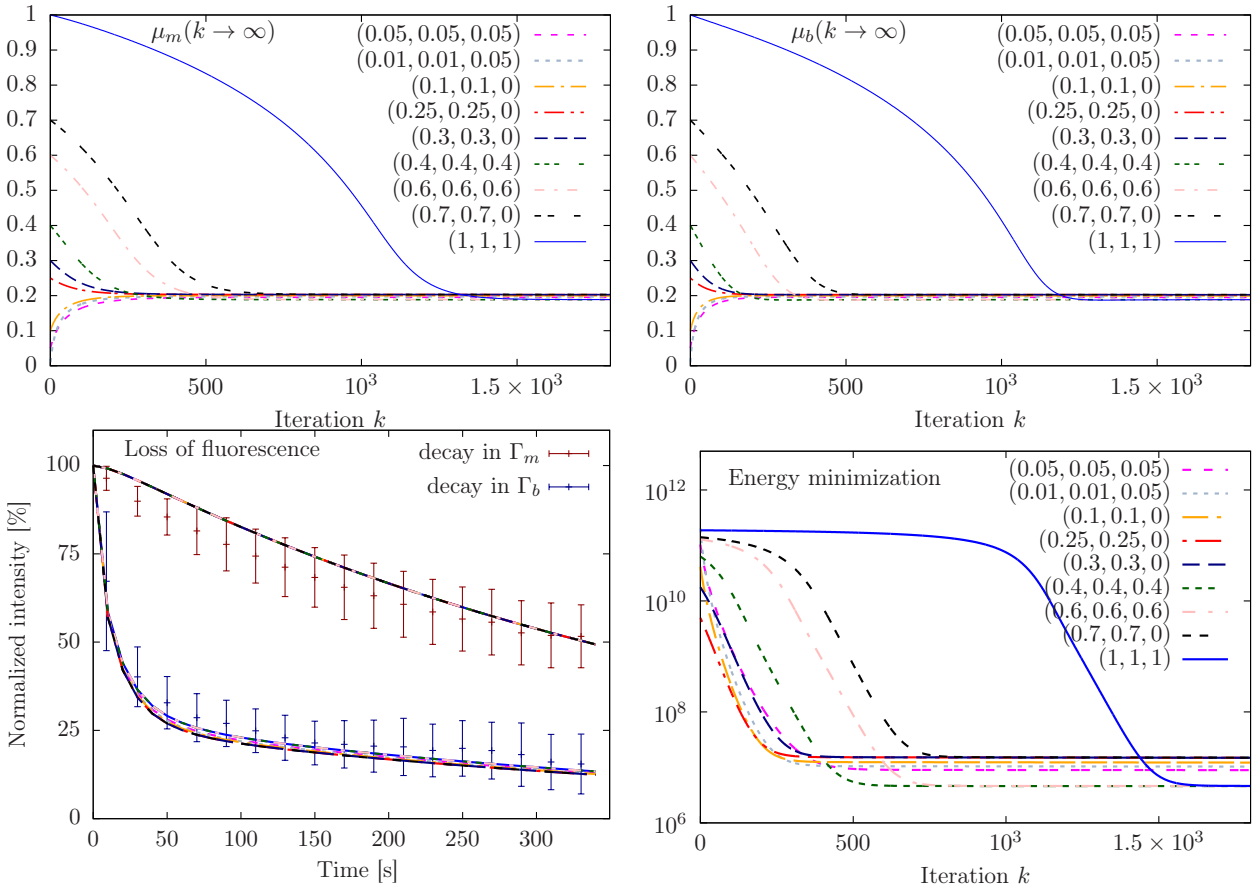

Figure 7 Example 2: Modification of estimates of control variables and optimal control solution for different choices of starting values for key parameters. Simulation parameters: $\alpha_{m,2} = \alpha_{b,2} = 0$, $\gamma_{m,2} = \gamma_{b,2} = 10^8$, $\delta = 10^{12}$, $\delta_m = \delta_b = \delta_r = 1$.

the iterative procedure converges and allows estimating the optimal parameters so that the solution corresponds to the target kinetics at final time T. In Fig. 6 (center), we plot using a semi-logarithmic scale the decrease of the cost functional as a function of the number of iterations for the two experiments, where $\mathcal{J}_\delta$ represents the energy term weighted by δ in (2.6) (similarly for the other terms). A first phase characterized by a rapid decrease is followed by a plateau characterizing convergence, where the optimal objective values are respectively 2.17×10^9 and 8.83×10^6. We also verified that the control parameters also converge; Fig. 6 (bottom) shows a rapid increase from the starting values with a following plateau with $\mu_m \approx \mu_b$. The estimated optimal sets of key parameters are $\mu_m = 0.232$, $\mu_b = 0.229$, $\mu_r = 0.124$ in the first test case, while $\mu_m = 0.195$, $\mu_b = 0.195$, $\mu_r = 0.078$ in the second case. Using the optimal parameters found, Fig. 5 provides snapshots of the numerical solution at the same times for the two aforementioned cases.

Sensitivity of the optimal control solution to the initial guesses:

We now investigate the sensitivity of the optimal control solution to the choice of starting values of the key parameters μ_m, μ_b and μ_r. We set $h = 0.043$ and use a $\mathbb{P}_1$ finite element approximations. The cost functional parameters are $\alpha_{m,2} = \alpha_{b,2} = 0$, $\gamma_{m,2} = \gamma_{b,2} = 10^8$, $delta = 10^{12}$, $\delta_m = \delta_b = \delta_r = 1$ so that more emphasis is placed on the solution matching targets at the final time T. We run several simulations for different choices of the starting values of the model parameters. Fig. 7 plots the changes in μ_m, μ_b, the objective functional $\mathcal{J}$ and the loss of fluorescence in Γ_m and Γ_b, showing that the optimal control solution is relatively insensitive to changes in the initial guesses. As expected, choosing a relatively far initialization of the model parameters results in slower convergence. Indeed, convergence is reached after 250 iterations for $\mu_m^0 = \mu_b^0 = \mu_r^0 = 0.05$, whereas it is reached after 1500 iterations for $\mu_m^0 = \mu_b^0 = \mu_r^0 = 1$.

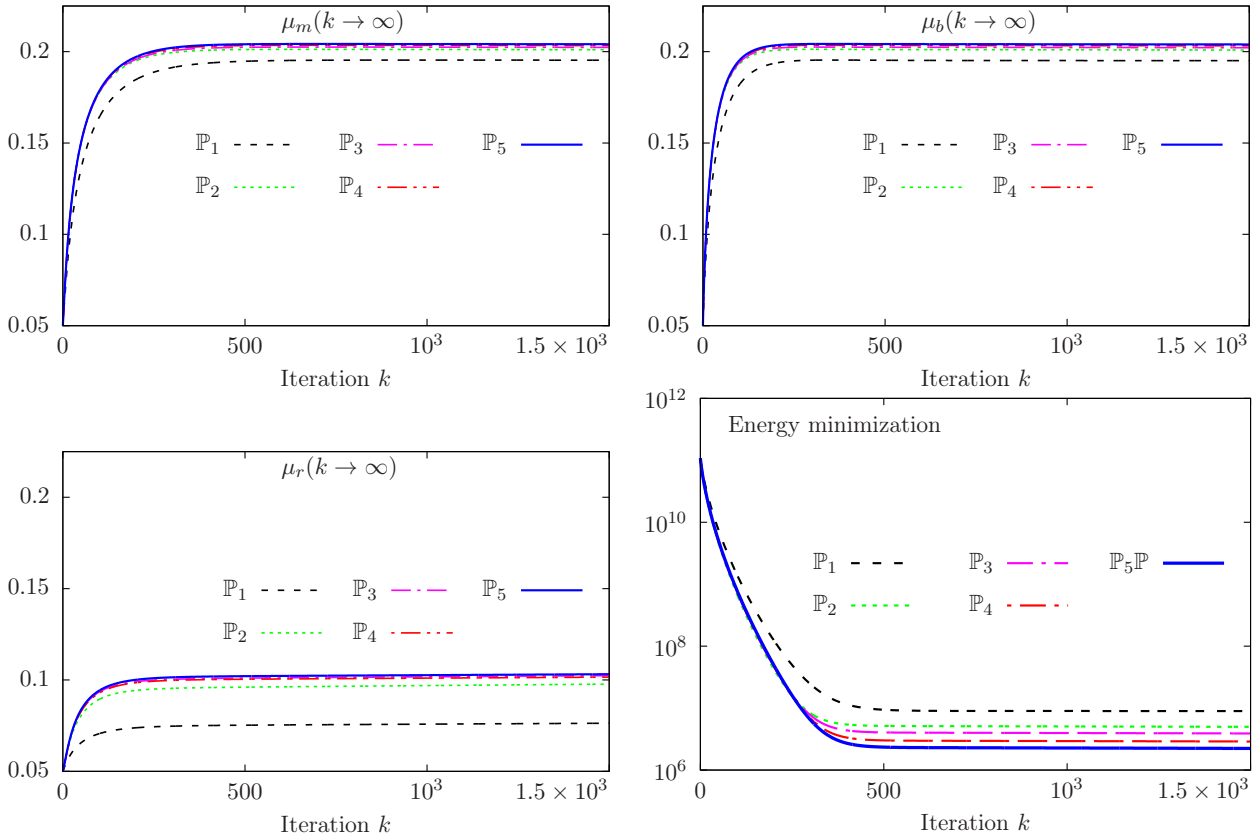

Figure 8 Example 2: Change in the estimates of control variables and cost functional for higher-order finite elements. Parameters: $\alpha_{m,2} = \alpha_{b,2} = 0$, $\gamma_{m,2} = \gamma_{b,2} = 10^8$, $\delta = 10^{12}$, $\delta_m = \delta_b = \delta_r = 1$ and $\mu_m^0 = \mu_b^0 = \mu_r^0 = 0.05$.

Convergence study for higher-order finite element approximations:

In this test case, we study the sensitivity of the optimal parameters to the choice of the finite element approximation. Let us consider higher-degree Lagrange polynomials $\mathbb{P}_\kappa, \kappa \geqslant 1$ and study the estimated optimal solutions with respect to the total number of degrees of freedom, referred to as Dof, for a fixed number of mesh elements.

For all simulations, we consider the following parameters: $\alpha_{m,2} = \alpha_{b,2} = 0, \gamma_{m,2} = \gamma_{b,2} = 10^8$, $\delta = 10^{12}$ and $\delta_m = \delta_b = \delta_r = 1$. The time step size is chosen small enough not to influence substantially the overall accuracy. The time horizon is $(0, T = 349)$. The evolution of the model parameters and the evolution of the energy cost with respect to the number of iterations are provided in Fig. 8, showing an overall convergence for higher degrees. The table 1 reports the optimal quantities calculated at convergence for higher polynomial degrees as well as the corresponding reference values, obtained by numerical continuation.

$\mathbb{P}_\kappa$	Dof	$\mu_m^\star(k \to \infty)$	$\mu_b^\star(k \to \infty)$	$\mu_r^\star(k \to \infty)$	$\mathcal{J}^\star(k \to \infty)$
$\mathbb{P}_1$	2407	0.195178	0.194918	0.0784062	8.83096E+6
$\mathbb{P}_2$	9622	0.201067	0.200895	0.0977545	4.98737E+6
$\mathbb{P}_3$	21647	0.202328	0.202163	0.102388	3.89932E+6
$\mathbb{P}_4$	38492	0.203342	0.203204	0.101571	2.89142E+6
$\mathbb{P}_5$	60127	0.204080	0.203959	0.103173	2.23366E+6
Reference values		0.206645	0.206725	0.102447	1.51009E+6

Table 1 Example 2: Convergence history for higher-order finite element approximations using $\mathbb{P}_\kappa$ with $\kappa \geqslant 1$.

Spatial convergence study:

Hereafter, we carry out a quantitative convergence study of the method with respect to the reference solution $q_{\mathrm{t,ref}}$ obtained by fitting the available measurement data. Let NTS design the number of time steps in each numerical simulation. We introduce the relative error corresponding to the temporal evolution of the quantity q_t and its rate of convergence as follows:

$$\|e_h\|_{\Gamma_b,2} = \left(\sum_{t=1}^{\mathrm{NTS}} |q_{\mathrm{t,ref}} - q_{\mathrm{t},h}|^2\right)^{1/2}, \quad \text{with } q_t = \int_{\Gamma_b} u_2(t,.) \quad \text{and ROC} = \frac{\log_{10}\left(\|e_h\|_{\Gamma_b,2}\right)}{\log_{10}(h)}.$$

The parameter h represents an average mesh size within a given mesh refinement level, while $q_{\mathrm{t},h}$ is an approximation of q using $\mathscr{T}_h$. For different values of NTS, we appropriately consider the standard linear interpolation applied to the solution q_t. The results in the table 2 show that the aforementioned quantity converges with a more than linear order of convergence in the norm l_2.

h	Dof	$\mu_m^\star(k\to\infty)$	$\mu_b^\star(k\to\infty)$	$\mu_r^\star(k\to\infty)$	ROC
0.094	1450	0.17493	0.17427	0.07649	2.77
0.060	2634	0.18637	0.18594	0.06838	2.33
0.043	4810	0.19538	0.19512	0.07592	2.08
0.038	7262	0.19930	0.19912	0.07714	1.85
0.029	12556	0.20756	0.20755	0.08490	1.65
0.019	26692	0.21499	0.21509	0.09372	1.53
0.014	28348	0.21669	0.21682	0.09342	1.53
0.009	102084	0.22317	0.22343	0.10016	1.37
0.007	150522	0.22501	0.22531	0.10168	1.31
0.004	368908	0.22799	0.22836	0.10386	1.19
Reference values		0.2305	0.2309	0.1084	–

Table 2 Example 3: Convergence history of same outputs with respect to spatial resolution. Simulation parameters: $\mathbb{P}_1$ Lagrange polynomials, $\alpha_{m,2} = \alpha_{b,2} = 0$, $\gamma_{m,2} = \gamma_{b,2} = 10^8$, $\delta = 10^{12}$, $\delta_m = \delta_b = \delta_r = 1$, and $\mu_m^0 = \mu_b^0 = \mu_r^0 = 0.05$.

4.3 | Example 3: Diffusion barrier in yeast endoplasmic reticulum

This test case concerns the numerical investigation of the empirical conclusions of the compartmentalization by diffusion barrier, where the optimization is performed over the time interval of each FLIP experiment. We perform numerical calculations using the data-driven model to investigate key model parameters in different cellular compartments, paying particular attention to the change in the cost functional. The effect of compartment size ratio on fluorescence kinetics will be explored afterwards in Example 4.

In this regard, we consider the setting and measurements of the aforementioned series of FLIP experiments described in Subsection 2.1, where photobleaching is either applied at the mother or bud compartments. The simulations are performed using a realistic unstructured ER mesh of nearly regular triangular elements. We choose an initial guess $\mu_m^0 = \mu_b^0 = \mu_r^0 = 0.43$ for the key parameters. We set the penalty parameter equal to $\epsilon = 10^{-10}$, while the Tykhonov regularization coefficients are $\delta_m = \delta_b = \delta_r = 1$.

The optimal control algorithm provided satisfactory results illustrating the convergence of the iterative procedure. Moreover, we follow the decay of the objective functional $\mathcal{J}^k$ with respect to the number of descent gradient iterations in Fig. 10 (left). The graph shows a rapid decrease in cost in an initial phase, followed by a horizontal plateau reached when the minimum is reached; That corresponds to the optimal objective functional obtained with the estimated optimal parameters.

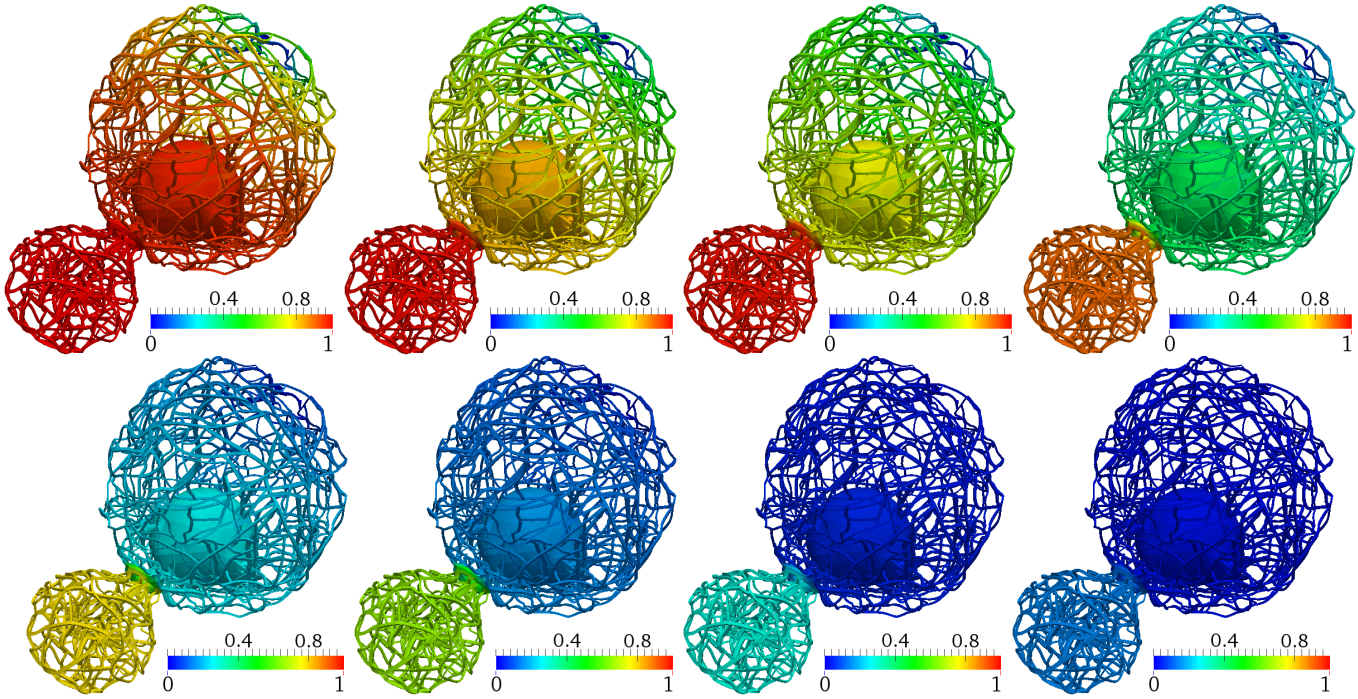

Figure 9 Example 3: Flipping in mother compartment. Snapshots showing fluorescence kinetics loss in numerical simulations with optimal model's parameters at times $t \in \{5, 15, 20, 50, 80, 110, 250, 355\}$.

The evolution of the adapted step length λ^k with respect to the number of iterations is reported in Fig. 10 (right). It shows in a first phase several fluctuations due to the adaptation of the step length to ensure the decrease of the cost functional, featuring here a rapid decrease. Subsequently, the variations of $\mathcal{J}$ are small, leading to lower and lower values of λ^k until it becomes lower than the tolerance threshold ϵ_λ when convergence is reached.

The change of model parameters with respect to the number of iterations is provided in Fig. 12. At convergence, the estimated model parameters are $\mu_m^\star = 0.661853$, $\mu_b^\star = 0.661895$ and $\mu_r^\star = 0.0312565$. To characterize the speed of protein diffusion in the ER membrane, the direct problem is then solved for both FLIP experiments using the estimated parameters. We evaluate the normalized intensity values throughout the times periods from the simulated kinetics of fluorescence in both bleached and unbleached cell compartments. We also show in Fig. 13 the target experimental data of the fluorescence signal over the specific

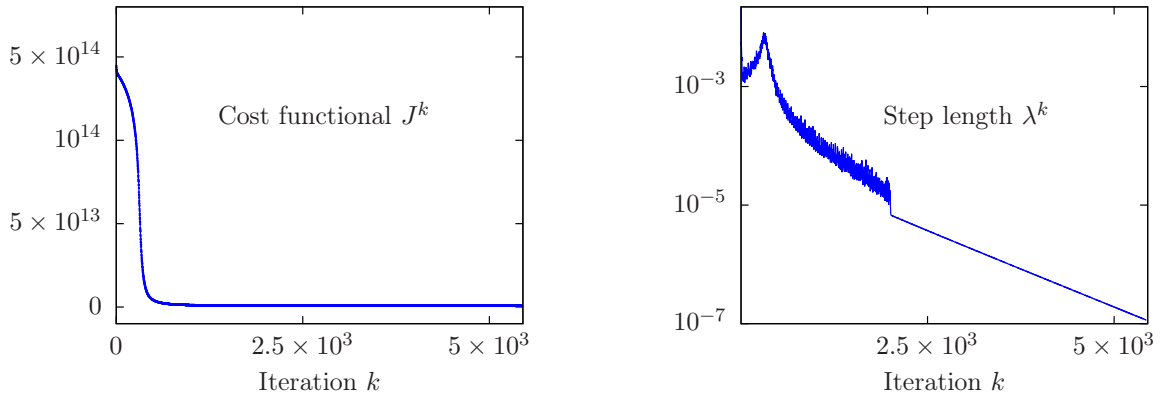

Figure 10 Example 3: (Left) Convergence towards the optimal objective function value versus the gradient descent iteration count k. (Right) Change in the step length λ with respect to the iteration count. The logarithmic scale is used on the y axis. Scaling coefficients: $\delta = 10^6$, $\alpha_{k,j} = 10^6$ and $\gamma_{k,j} = 0\ \forall k \in \{m, b\}$ and $j \in \{1, 2\}$, and $\delta_m = \delta_b = \delta_r = 1$. Starting values for key parameters: $\mu_m^0 = \mu_b^0 = \mu_r^0 = 0.43$.

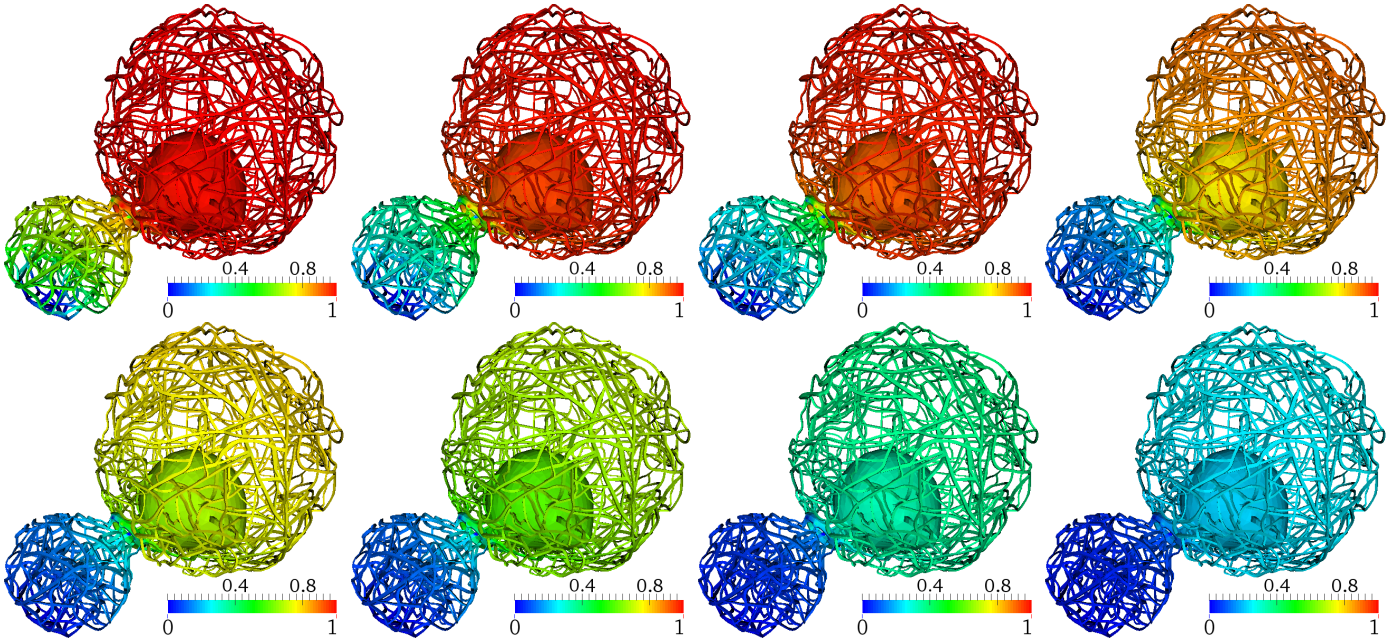

Figure 11 Example 3: Flipping in bud compartment. Snapshots showing fluorescence kinetics loss in numerical simulations with optimal model's parameters at times $t \in \{5, 15, 20, 50, 80, 110, 250, 355\}$.

measurement instants, together with its maximum and minimum values. This shows a good agreement between the numerical results and the experimental measurements.

The estimated optimal control parameters satisfy $\mu_m^\star/\mu_b^\star \approx 1.0$ and $\mu_m^\star/\mu_r^\star \approx 21.2$. That is, the numerical results reveal that the diffusion of the reporter protein is similarly fast in the mother and in the bud compartments. However, it is 21 times slower in the barrier zone at the level of the bud neck. Numerical results are in agreement with the conclusions of many biologists that a physical diffusion barrier exists between the main compartments, whereas the protein Sec61-GF moves at similar speeds in the mother and bud compartments, see e.g. [9]. Consequently, the restricted diffusion in the bud neck region helps to slow the loss of fluorescence in the unbleached compartment in each FLIP experiments. From a biological point of view, the bud neck area features a specific morphology and contributes primarily, and among other things, to the retention of damage and aging factors between the mother and daughter cell, as mentioned above. To our knowledge, this is the first numerical study quantitatively

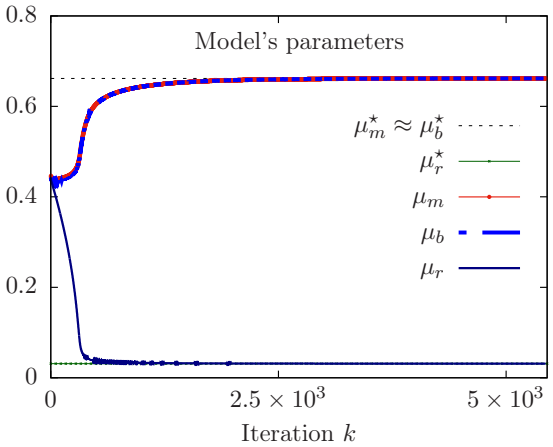

Figure 12 Example 3: Change in the estimates of control variables versus the iteration count k. Scaling coefficients: $\delta = 10^6$, $\alpha_{k,j} = 10^6$ and $\gamma_{k,j} = 0$ for $k \in \{m, b\}$ and $j \in \{1, 2\}$, and $\delta_m = \delta_b = \delta_r = 1$. Initial guesses: $\mu_m^0 = \mu_b^0 = \mu_r^0 = 0.43$.

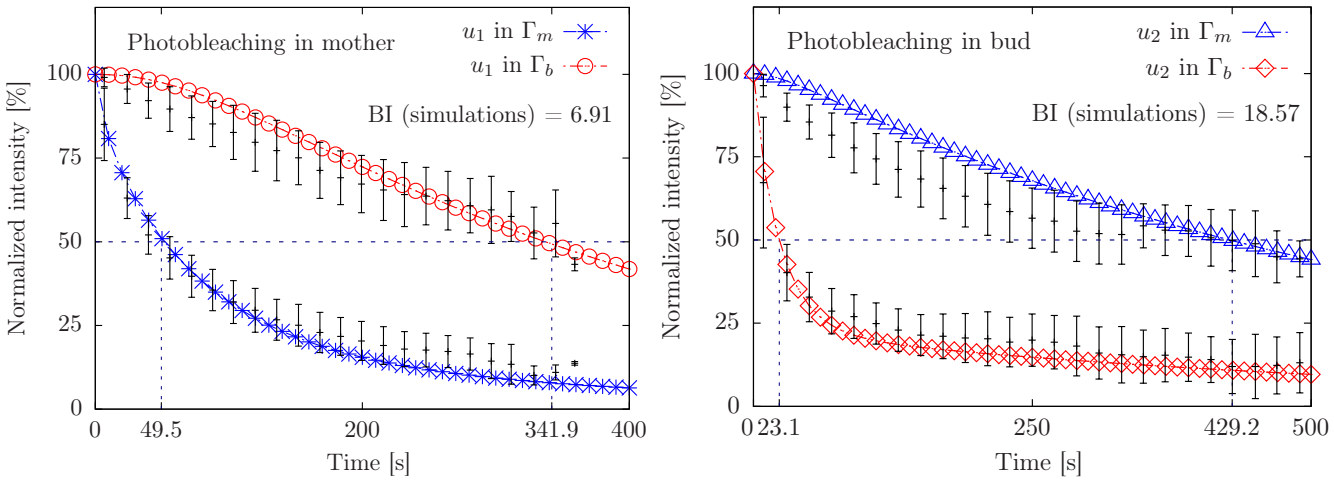

Figure 13 Example 4: Time evolution of the kinetics of fluorescence, obtained with the estimated optimal parameters, compared to the experimental data. (Left) Photobleaching applied to mother cortex. (Right) Photobleaching applied to the bud. Error bars indicate the standard deviation SD after averaging 20 different data measurements. Mean ± SD.

confirming the diffusion barrier theory. However, we are still far from a high-fidelity mathematical description characterizing the intrinsic processes underlying such barriers.

4.4 | Example 4: Barrier index and dependency on compartments' size ratio

Thereafter, we explore the effect of compartment size on fluorescence kinetics. An index of great importance to biologists is the Barrier Index, referred to as BI. We first define $T_{1/2}$ as the time corresponding to a concentration equal to 50% of the initial concentration before photobleaching in a given compartment, as shown graphically in Fig 13. The BI represents the ratio of the times required to lose 50% of the fluorescence signal in the unbleached compartment compared to the bleached compartment.

An agreement in the calculation of the barrier index between the photobleached and unbleached compartments between the numerical and experimental results is obtained. Remark that the BI reaches much higher values (18.22 ± 1.90 experimentally and 18.572 numerically) when photobleaching is applied to the bud than when it is applied to the mother (7.76 ± 2.27 experimentally and 6.907 numerically), see Fig 14. The biologists rationalized that this might simply be due to the fact that the ER volume in the bud is smaller than that in the mother cell, leading to a much more rapid depletion of the smaller compartment upon FLIP.

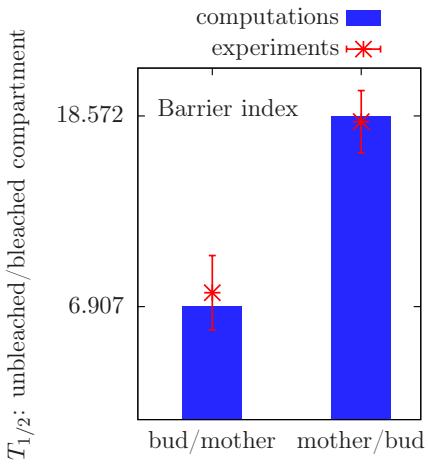

Figure 14 Example 4: Bar chart representing the $T_{1/2}$ of the unbleached compartment over the $T_{1/2}$ of the bleached compartment in the experimented in comparison to the simulated data. Mean ± SD.

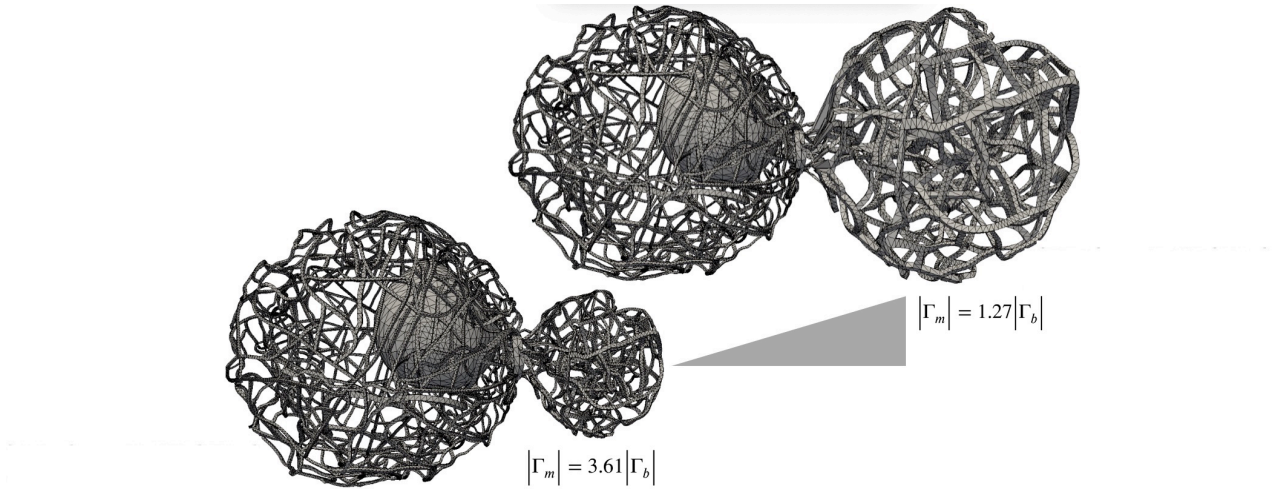

Figure 15 Example 4: (Left) ER mesh featuring a size of the bud nearly identical to the size of the mother cell. (Right) Segmented realistic realistic geometry of the yeast ER.

In order to test whether this explanation indeed explains the yeast observations, the dependence between the compartment size ratio and the barrier index is studied numerically. We calculate how the observed BI would change when the relative volume of mother and bud is allowed to vary. Using the segmented ER geometry, we generate different meshes without changing the ER organization in the mother cortex but where the bud is increasingly bigger, until reaching almost the size of the mother compartment, see Fig 15. The surface meshes are subsequently remeshed in order to optimize the quality of the mesh for carrying out finite element calculations.

We consider the optimal parameters $\mu_m^\star$, $\mu_b^\star$ and $\mu_r^\star$ found previously. Parallel FLIP experiments were then simulated in each of these meshes, FLIPing either the mother or the bud compartment. In each geometry, the values of the BI obtained by photobleaching in the mother and in the bud are then compared. Whereas the ratio between the BI in the bud divided by the BI in the mother is high as long as the bud domain is significantly smaller than the mother cell, this ratio becomes close to 1 as the size of the bud approaches the size of the mother, see Fig. 16. A noticeable consequence is that, at least in budding yeast cell, the difference in BI depending on the place of photobleaching reflects the fact that (i) the ER membrane is compartmentalized and (ii) one compartment is smaller than the other.

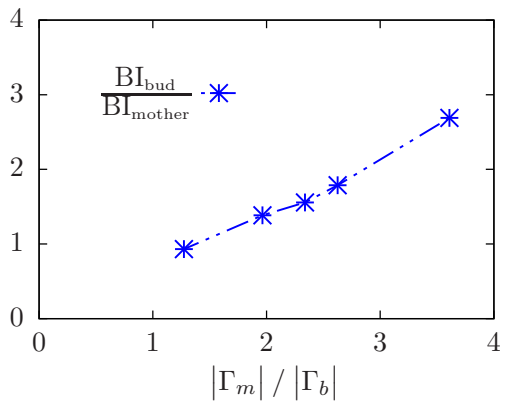

Figure 16 Example 4: Change in the ratios BI_{bud}/BI_{mother} when the size of the bud increases relative to the size of the mother. It tends to 1 for similar sizes of ER compartments.

5 | CONCLUSIONS

This contribution presents a numerical framework for the modeling of the kinetics of fluorescently tagged molecules on the endoplasmic reticulum in asymmetrically dividing yeast cell. Using the Fluorescence Loss In Photobleaching technique, experiments are carried out in laboratory and provide measurement data on the decrease in the level of fluorescence in the different cellular compartments. To study the anisotropic molecular diffusion, we present a data-driven model based on the use of partial differential equations constrained optimization. Optimality conditions are derived and a gradient descent algorithm is used to estimate the diffusion parameters in the different cellular compartments. We address the main features of the method and we provide numerical simulations with the aim of providing numerical evidence of compartmentalization in the ER membrane. Our computational model supports some biological conclusions indicating that the exchange of membrane proteins between mother and bud compartments is very slow, almost 20 times slower, compared to the diffusion of proteins into each compartment due to some surface diffusion limitations at the bud-neck zone.

This compartmentalization is also conserved in a broad range of cellular contexts, such as mouse neural stem cells and the early C. elegans embryo, and contributes to processes as diverse as the confinement of protein aggregates during aging and the patterning of developing embryos. Further improvements are needed to better explore the compartmentalisation in budding cells, while accounting for high fidelity mathematical descriptions. This is part of an ongoing work to explore concordant hypotheses for anisotropic exchange of ER proteins in yeast and cardiac myocytes[46], with a more accurate mathematical formalism accounting for uncertainty quantification in the solution and the sensitivity of data noise on model parameters.

ACKNOWLEDGEMENT

A. Laadhari gratefully acknowledges the financial support by KU through the grant FSU-2021-027.

Conflict of interest

The authors declare no potential conflict of interests.

References

1. Puhka M, Vihinen H, Joensuu M, Jokitalo E. Endoplasmic reticulum remains continuous and undergoes sheet-to-tubule transformation during cell division in mammalian cells . *Journal of Cell Biology* 2007; 179(5): 895–909. doi: 10.1083/jcb.200705112

2. Dayel M, F HE, Verkman AS. Diffusion of green fluorescent protein in the aqueous-phase lumen of endoplasmic reticulum. *Biophys. J.* 1999; 76: 2843–2851.

3. Lippincott-Schwartz J, Snapp E, Kenworthy A. Studying protein dynamics in living cells. *Nature Reviews Molecular Cell Biology* 2001; 2(6): 444–456. doi: 10.1038/35073068

4. Lippencott-Schwartz J, Altan-Bonnet N, Patterson GH. Photobleaching and photoactivation: following protein dynamics in living cells. *Nature Cell Biology* 2003; 5: S7–S14.

5. English A, Voeltz G. Endoplasmic reticulum structure and interconnections with other organelles. *Cold Spring Harbor Perspectives in Biology* 2013; 5: a013227. doi: 10.1101/cshperspect.a013227

6. Caudron F, Barral Y. Septins and the Lateral Compartmentalization of Eukaryotic Membranes. *Developmental Cell* 2009; 16(4): 493–506. doi: 10.1016/j.devcel.2009.04.003

7. West M, Zurek N, Hoenger A, Voeltz GK. A 3D analysis of yeast ER structure reveals how ER domains are organized by membrane curvature. *The Journal of cell biology* 2011; 132(2): 333–346.

8. Clay L, Caudron F, Denoth-Lippuner A, et al. A sphingolipid-dependent diffusion barrier confines ER stress to the yeast mother cell. *eLife* 2014; 3: e01883. doi: 10.7554/eLife.01883

9. Luedeke C, Frei SB, Sbalzarini I, Schwarz H, Spang A, Barral Y. Septin-dependent compartmentalization of the endoplasmic reticulum during yeast polarized growth. *Journal of Cell Biology* 2005; 169(6): 897–908. doi: 10.1083/jcb.200412143

10. Tabas I, Ron D. Integrating the mechanisms of apoptosis induced by endoplasmic reticulum stress. *Nature Cell Biology* 2011; 13(3): 184–190. doi: 10.1038/ncb0311-184

11. Shcheprova Z, Baldi S, Frei S, Gonnet G, Barral Y. A mechanism for asymmetric segregation of age during yeast budding. *Nature* 2008; 454(7205): 728–734. doi: 10.1038/nature07212

12. Douglas J, Russell TF. Numerical Methods for Convection-Dominated Diffusion Problems Based on Combining the Method of Characteristics with Finite Element or Finite Difference Procedures. *SIAM Journal on Numerical Analysis* 1982; 19(5): 871–885. doi: 10.1137/0719063

13. Martínez A, Rodríguez C, Vázquez-Méndez ME. Theoretical and Numerical Analysis of an Optimal Control Problem Related to Wastewater Treatment. *SIAM Journal on Control and Optimization* 2000; 38(5): 1534–1553. doi: 10.1137/S0363012998345640

14. Zhou Z, Yan N. The local discontinuous Galerkin method for optimal control problem governed by convection diffusion equations. *International Journal of Numerical Analysis and Modeling* 2010; 7: 681–699.

15. Zhu J, Zeng Q. A mathematical formulation for optimal control of air pollution. *Science in China Series D: Earth Sciences* 2003; 46(10): 994–1002. doi: 10.1007/BF02959394

16. Kim D, Park EJ. A posteriori error estimators for the upstream weighting mixed methods for convection diffusion problems. *Computer Methods in Applied Mechanics and Engineering* 2008; 197(6): 806–820. doi: 10.1016/j.cma.2007.09.009

17. Hogea C, Davatzikos C, Biros G. An image-driven parameter estimation problem for a reaction–diffusion glioma growth model with mass effects. *Journal of Mathematical Biology* 2008; 56(6): 793–825. doi: 10.1007/s00285-007-0139-x

18. Jiang CS, Zhang YX. A parameter identification and inversion method for a class of reaction-diffusion systems. *Control Theory Appl.* 2000; 17: 193 – 197.

19. Lenhart S, Workman JT. Optimal Control Applied to Biological Models (1st ed.). *Mathematical and Computational Biology Series, Chapman and Hall/CRC* 2007. doi: 10.1201/9781420011418

20. Garvie MR, Trenchea C. Optimal Control of a Nutrient-Phytoplankton-Zooplankton-Fish System. *SIAM Journal on Control and Optimization* 2007; 46(3): 775–791. doi: 10.1137/050645415

21. Gunzburger MD. *Perspectives in Flow Control and Optimization.* Society for Industrial and Applied Mathematics . 2002

22. Liao GG, Cai X, Fleitas D, Luo X, Wang J, Xue J. Optimal control approach to data set alignment. *Applied Mathematics Letters* 2008; 21(9): 898-905. doi: 10.1016/j.aml.2007.09.011

23. Becker R, Vexler B. Optimal control of the convection-diffusion equation using stabilized finite element methods. *Numerische Mathematik* 2007; 106(3): 349–367. doi: 10.1007/s00211-007-0067-0

24. Ruo L, Wenbin L, Heping M, Tao T. Adaptive Finite Element Approximation for Distributed Elliptic Optimal Control Problems. *SIAM Journal on Control and Optimization* 2002; 41(5): 1321–1349. doi: 10.1137/S0363012901389342

25. Yan N, Zhou Z. A Priori and a Posteriori Error Estimates of Streamline Diffusion Finite Element Method for Optimal Control Problem Governed by Convection Dominated Diffusion Equation. *Numerical Mathematics: Theory, Methods and Applications* 2008; 1(3): 297–320.

26. Yan N, Zhou Z. A priori and a posteriori error analysis of edge stabilization Galerkin method for the optimal control problem governed by convection-dominated diffusion equation. *Journal of Computational and Applied Mathematics* 2009; 223(1): 198–217. doi: 10.1016/j.cam.2008.01.006

27. Khaksar-E Oshagh M, Shamsi M. Direct pseudo-spectral method for optimal control of obstacle problem – an optimal control problem governed by elliptic variational inequality. *Mathematical Methods in the Applied Sciences* 2017; 40(13): 4993–5004. doi: https://doi.org/10.1002/mma.4366

28. Hollis SL, Martin RH, Pierre M. Global Existence and Boundedness in Reaction-Diffusion Systems. *SIAM Journal on Mathematical Analysis* 1987; 18(3): 744–761. doi: 10.1137/0518057

29. Garvie MR, Trenchea C. Identification of Space-Time Distributed Parameters in the Gierer–Meinhardt Reaction-Diffusion System. *SIAM Journal on Applied Mathematics* 2014; 74(1): 147–166. doi: 10.1137/120885784

30. Casas E, De Los Reyes JC, Tröltzsch F. Sufficient Second-Order Optimality Conditions for Semilinear Control Problems with Pointwise State Constraints. *SIAM Journal on Optimization* 2008; 19(2): 616–643. doi: 10.1137/07068240X

31. Hoppe F, Neitzel I. Optimal Control of Quasilinear Parabolic PDEs with State-Constraints. *SIAM Journal on Control and Optimization* 2022; 60(1): 330–354. doi: 10.1137/20M1383951

32. Yücel H, Stoll M, Benner P. A discontinuous Galerkin method for optimal control problems governed by a system of convection-diffusion PDEs with nonlinear reaction terms. *Computers and Mathematics with Applications* 2015; 70(10): 2414–2431. doi: https://doi.org/10.1016/j.camwa.2015.09.006

33. Betts JT. *Practical Methods for Optimal Control Using Nonlinear Programming, Third Edition*. Philadelphia, PA: Society for Industrial and Applied Mathematics . 2020

34. Mills WH. Algorithmic Methods in Optimal Control (W. A. Gruver and E. Sach). *SIAM Review* 1983; 25(4): 579–580. doi: 10.1137/1025134

35. Kelley CT. *Iterative Methods for Optimization*. Society for Industrial and Applied Mathematics . 1999

36. Laadhari A, Székely G. Eulerian finite element method for the numerical modeling of fluid dynamics of natural and pathological aortic valves. *Journal of Computational and Applied Mathematics* 2017; 319: 236–261. doi: https://doi.org/10.1016/j.cam.2016.11.042

37. Laadhari A, Quarteroni A. Numerical modeling of heart valves using resistive Eulerian surfaces. *International Journal for Numerical Methods in Biomedical Engineering* 2016; 32(5): e02743. e02743 cnm.2743doi: https://doi.org/10.1002/cnm.2743

38. Perić D, Owen DRJ. Computational model for 3-D contact problems with friction based on the penalty method. *International Journal for Numerical Methods in Engineering* 1992; 35(6): 1289–1309. doi: 10.1002/nme.1620350609

39. Janela, J , Lefebvre, A , Maury, B . A penalty method for the simulation of fluid - rigid body interaction. *ESAIM: Proc.* 2005; 14: 115–123. doi: 10.1051/proc:2005010

40. Astorino M, Hamers J, Shadden SC, Gerbeau JF. A robust and efficient valve model based on resistive immersed surfaces. *International Journal for Numerical Methods in Biomedical Engineering* 2012; 28(9): 937–959. doi: https://doi.org/10.1002/cnm.2474

41. Tikhonov KAN, Goncharsky AV, Stepanov VV, Yagola AG. Numerical Methods for the Solution of Ill-Posed Problems. In: . 328 of *Mathematics and Its Applications*. Springer Dordrecht. 1995 (pp. 253)

42. Engl HW, Hanke M, Neubauer A. *Regularization of Inverse Problems*. Mathematics and Its Applications, Springer Dordrecht. 1 ed. 2000. Volume 375, ISBN 978-0-7923-6140-4.

43. Vogel CR. *Computational Methods for Inverse Problems*. Society for Industrial and Applied Mathematics . 2002

44. Saramito P. *Efficient C++ Finite Element computing with Rheolef*. Grenoble, France: CNRS-CCSD ed. . 2020. HAL version: v15. Accessed: 26.09.22.

45. Deckelnick K, Dziuk G, Elliott CM, Heine CJ. An h-narrow band finite-element method for elliptic equations on implicit surfaces. *IMA Journal of Numerical Analysis* 2010; 30(2): 351–376. doi: 10.1093/imanum/drn049

46. Laadhari A, Ruiz-Baier R, Quarteroni A. Fully Eulerian finite element approximation of a fluid-structure interaction problem in cardiac cells. *International Journal for Numerical Methods in Engineering* 2013; 96(11): 712–738. doi: https://doi.org/10.1002/nme.4582

How to cite this article: Laadhari A., Barral Y., and Székely G., A data-driven model for endoplasmic reticulum membrane compartmentalization in budding yeast cells, *Math Methods Appl Sci*, submitted.